Arterial microanatomy determines the success of energy-based renal denervation in controlling hypertension

Citation: Tzafriri, Abraham R., John H. Keating, Peter M. Markham, Anna-Maria Spognardi, James R. L. Stanley, Gee Wong, Brett G. Zani, Debby Highsmith, Patrick O'Fallon, Kristine Fuimaono, Felix Mahfoud, and Elazer R. Edelman. "Arterial Microanatomy Determines the Success of Energy-Based Renal Denervation in Controlling Hypertension." Science Translational Medicine 7, no. 285 (April 29, 2015): 285ra65–285ra65.

As Published: http://dx.doi.org/10.1126/scitranslmed.aaa3236

Publisher: American Association for the Advancement of Science (AAAS)

Persistent URL: http://hdl.handle.net/1721.1/102941

Version: Author's final manuscript: final author's manuscript post peer review, without publisher's formatting or copy editing

HHS Public Access

Author manuscript

Sci Transl Med. Author manuscript; available in PMC 2015 October 28.

Published in final edited form as:

Sci Transl Med. 2015 April 29; 7(285): 285ra65. doi:10.1126/scitranslmed.aaa3236.

Arterial microanatomy determines the success of energy-based renal denervation in controlling hypertension

Abraham R. Tzafriri[1], **John H. Keating**[1], **Peter M. Markham**[1], **Anna-Maria Spognardi**[1], **James R. L. Stanley**[1], **Gee Wong**[1], **Brett G. Zani**[1], **Debby Grunewald**[2], **Patrick O'Fallon**[2], **Kristine Fuimaono**[2], **Felix Mahfoud**[3], and **Elazer R. Edelman**[4,5]

[1]Departments of Applied Sciences and Pathology, CBSET, Lexington, MA

[2]Cordis/Biosense Webster, Inc. a Johnson & Johnson Company, Irwindale, CA

[3]Department of Internal Medicine III, Saarland University, Homburg/Saar, Germany

[4]Institute for Medical Engineering and Science, MIT, Cambridge, MA

[5]Brigham and Women's Hospital, Boston, MA

Abstract

Renal Denervation (RDN) is a treatment option for patients with hypertension resistant to conventional therapy. Clinical trials have demonstrated variable benefit. To understand the determinants of successful clinical response to this treatment, we integrated porcine and computational models of intravascular radiofrequency RDN. Controlled single-electrode denervation resulted in ablation zone geometries that varied in arc, area and depth, depending on the composition of the adjacent tissue substructure. Computational simulations predicted that delivered power density was influenced by tissue substructure, and peaked at the conductivity discontinuities between soft fatty adventitia and water rich tissues (media, lymph nodes etc.), not at the electrode-tissue interface). Electrode irrigation protected arterial wall tissue adjacent to the electrode by clearing heat that diffuses from within the tissue, without altering peri-arterial ablation. Seven days after multi-electrode treatments, renal norepinephrine and blood pressure were reduced. Blood pressure reductions were correlated with the size-weighted number of degenerative nerves, implying that the effectiveness of the treatment in decreasing hypertension depends on the extent of nerve injury and ablation, which in turn are determined by the tissue microanatomy at the electrode site. These results may explain the variable patient response to RDN and suggest a path to more robust outcomes.

Correspondence: Rami Tzafriri, PhD, 500 Shire Way, Lexington, MA – 02421, Phone: 781-541-5589, Fax: 781-541-5656, rtzafriri@cbset.org.

Competing interests: The other authors declare that they have no competing interests.

Author contributions: Conception, design and study direction: AS, ART, BZ, ERE, FM, JHK, JRLS, KF, PMM. Animal studies: AS, GW, JHK, JRLS. Computational modeling: ART. Data analysis: ART, GW, JHK, PMM. Manuscript write-up: AS, ART, ERE, FM, JHK.

Supplementary Materials
Numerical analysis

INTRODUCTION

The sympathetic nervous system regulates cardiac output, blood pressure (BP) and volume, electrolyte balance and body fluid composition. Elevated sympathetic activity contributes to the pathophysiology of almost all forms of hypertension (1), which is exacerbated with comorbidities such as renal disease (2). Thus the renal sympathetic pathway is an attractive target for the treatment of hypertension and potentially other diseases characterized by increased sympathetic activity. Prior to the development of antihypertensive drugs, surgical sympathectomy was a last resort therapy (3). Although a fraction of patients (40–60%) had lower BP after surgical sympathectomy (3), these procedures were non-specific and associated with high morbidity and complications.

The current refinement of this procedure, catheter-based renal denervation (RDN) more selectively disrupts renal sympathetic nerves with shorter procedural and recovery times. Proof-of-concept and short-term safety of radiofrequency (RF)-based RDN were demonstrated in the first and second SYMPLICITY HTN (Renal Sympathetic Denervation in Patients with Treatment-Resistant Hypertension) trials, which tested the effectiveness of a dedicated RF ablation catheter (4–7). Despite early successes and positive expectations, the incidence of non-responsive patients remains stubbornly high (8–9) and as yet unexplained. Moreover, the recently published prospective, single-blind, randomized SYMPLICITY HTN-3 trial failed to show significant difference in reduction of systolic BP in patients with resistant hypertension 6 months after RDN compared to sham controls (10). To some this suggested that sympathetic activation is not universal to hypertension (9, 11) and to others that some effects of RDN remain uncontrolled and poorly understood (especially given reports that renal artery innervation patterns are assymetric) (12–14). Indeed, intravascular RDN can injure the intima and cause microthrombi (15–16), raising long-term safety concerns. The local concentration of heat might preferentially injure the most susceptible tunica intima and endothelium. Further, norepinephrine spillover measurements in SYMPLICITY HTN-1 patients suggest incomplete neural ablation by mono-polar single electrodes (17), and postmortem analysis from a patient 12 days after bilateral Symplicity RDN (18) showed incomplete neural ablation.

In the current study, therefore, we characterized and sought to explain the ablation patterns achieved by intravascular conventional and irrigated RDN through the use of animal and computational models.

RESULTS

Seven Yorkshire swine were treated bilaterally and 10 Yucatan swine unilaterally with the Renlane catheter, sacrificed 7 days after RDN, and their tissues sectioned for histopathology. Unilateral treatments were delivered by 5 irrigated electrodes, and BP measured under anesthesia before and 7 days after RDN. Of the 14 bilaterally treated arteries, 8 were treated with 5 electrodes and irrigation, and 6 with only 2 or 3 non neighboring discrete electrodes with (n=3) or without (n=3) irrigation, to achieve discrete, non-overlapping ablation zones. When all 5 electrodes are activated, the Renlane catheter delivers treatments along a helix

that mimics the recommended protocol for sequential single-electrode treatments with the Simplicity device (8).

Non-irrigated discrete electrodes: treatment effects and ablation geometries

We characterized the entire ablation zone for each of the treatment sites by activating non-neighboring electrodes (without irrigation) (Fig 1A,B), and then step-sectioned the treated vessels (Fig 1 C–G). Application of the RF stimulus was invariably injurious, with coagulative necrosis extending through the electrode-adjacent arterial media and into surrounding peri-arterial tissue. Treatment resulted in stretching and thinning of the arterial wall (Fig 1 C, E and Gi). Quantitative morphometry performed on the maximal injury zones revealed that 40.1±6.7% of the luminal circumference, 43.4±5.5% of the circumference of the external elastic lamina (EEL) and 36.1±6.6% of medial area were affected. Treated arterial walls were thinned by 25.7±22.6%. Thus, blood flow did not efficiently carry away enough heat to protect the arterial wall surrounding the point of contact with the non-irrigated RF electrodes.

Tissue sections of these regions showed complex peri-arterial anatomy, with muscle or fibrous tissue located posterior to the artery, peritoneum and often large veins on the anterior side, and lymph nodes and blood vessels in various locations (Fig 1, C–G). Ablation zone orientations, shapes and dimensions were highly variable (Table 1) and tended to end abruptly at the periphery of neighboring veins and arteries (Fig 1 C, D, G). In total, 43±13% of nerves in the sections with the maximal ablation zone area were affected, with the majority of these injured nerves located within the traced ablation zones (Table 1). Consistent with the moderate percentage of affected nerves in discrete electrode treatments, associated renal NEPI levels (574.0±173.1 ng/g, 3 kidneys, 2 samples each), an index of sympathetic innervation of the kidney, were comparable to those reported at baseline (19), 649±161 ng/g.

Computational modeling of ablation geometries

To understand how local tissue composition affected power distribution from the RF electrode, we performed computational simulations of heat distribution and tissue ablation after intravascular treatment with a single electrode. When we assumed that arterial and peri-arterial tissue were homogeneous, both current density (J) and power density (J^2/σ) peaked at the electrode-tissue interface and declined steeply with increasing distance from the electrode. Temperature was predicted to distribute symmetrically around the energy source (Fig 2 A,B), peaking at the electrode-tissue interface and declining steeply with distance, attaining body temperature 1 cm away from the electrode. However, such temperature maps were inconsistent with the distribution of the observed lesions. We reasoned that this could be because the assumption that the tissues were homogeneous, which led to the prediction of steep monotonic temperature declines(20), was inaccurate. Rather, renal arteries and their surrounding tissues are complex in structure, with heterogeneous electrical conductivities and thermal absorption properties. Therefore we examined how individual tissue element affected model prediction of observed lesion geometry.

The EEL delineates the transition between the water-rich, high-conductivity media and fatty, low conductivity adventitial tissue. As current density varies continuously across such interfaces of conductivity discontinuity, RF power distributed asymmetrically across the EEL (Fig 2C), with more power being delivered to the more resistive adventitial tissue. As a result, power density first peaked at the electrode-tissue interface, declined in the media, then achieved an even higher peak at the EEL, slowly declining in the adventitia. Tissue temperature was determined by a balance between locally delivered power and diffusion-mediated heat efflux towards the cooler lumen and tissue peripheries (Fig 2D). Luminal blood flow cleared heat from the media and slightly beyond the EEL, but only after sufficient time had elapsed for heat to diffuse from the tissue site towards the lumen (compare Fig. 2D 10 sec and 2D 30 sec). Because there is a time lag for heat clearance by blood and the rate of luminal flow is finite, tissue temperatures adjacent to the electrode remain above ambient (37°C) for almost 20 sec after the treatment (Fig 2D). Consequently, even though the adjacent blood flow removed heat, the time-averaged temperature exceeded the threshold for injury in the vicinity of the electrode, up to 4.3 mm deep into the adventitia and even lateral to the electrodes (Fig 2E). The predicted mushroom-like pattern of injury reflects a balance between heat diffusion, which is nearly isotropic, and heat clearance near the lumen. The localization of injury to the luminal wall in the immediate vicinity of the electrode is a result of the electrode shielding the apposed mural tissue from the cooling effect of blood perfusion. If blood flow is set to zero in the model, as is the case during the inflation of certain RF balloons (8) (but not the Renlane catheter), the pattern of injury is determined solely by thermal diffusion (Fig 2F).

We assessed the influence of high conductivity anatomical structures (HCAS), such as lymph nodes, skeletal muscle and associated fibrous tissue, and then tested the role of HCAS that are also heat sinks (HS) such as blood vessels. Simulations predicted that ablation zone geometry was profoundly sensitive to the distance and orientation of lymph nodes relative to the treating electrode (Fig 3 vs Fig 2E). Similarly, lateral fibrous muscle sheaths (Fig 1C–D) drew the electric field and substantially increased the lateral and circumferential extent of the ablation (Fig 4A vs Fig 2E). When we added a lateral vein between the artery wall and the fibrous sheath (Fig 1C–D), venous blood flow efficiently cleared heat from the region bounded by the two blood vessels (Fig 4B). Thus, heat reached the fibrous sheath only via diffusion through surrounding soft tissue, resulting in an asymmetric ablation surrounding this vessel (HCAS/HS). Addition of a smaller lateral vein on the opposite side of the electrode (Fig 4C) or of two small distal veins (Fig 4D) siphoned heat from the vicinity of the peri-arterial blood vessels and blocked the peri-arterial spread of the ablation in the locally cooled zones. Thus, the predicted influence of peri-arterial blood vessels on ablation geometry depended on vessel size and orientation relative to the treating electrode and other neighboring HCAS. However, beyond a threshold distance the effects of peri-arterial blood vessels on the ablation zone become negligible (Fig 4E). When the HCAS and HS are accounted for (Fig 4F), the predicted ablation pattern realistically mimics the observed geometry of the actual ablation (Fig 1F). Accounting for the total HS capacity and the relative distance from the electrodes was critical. When HCAS or HS covered a large area directly adjacent to the electrode, siphoning of heat could significantly

reduce lesion size (Fig 4G vs Fig 4F) and in certain cases (Fig 4H) potentially negate any effect on the adjacent nerves.

Irrigated electrodes: ablation geometries and treatment effects

The prediction by our computational model that peak power is achieved beyond the electrode-tissue interface implies that the effects of the RF stimulus on the arterial wall are more easily ameliorated by heat diffusion than are the peri-arterial effects, paving the way for optimal targeting of RF power and wall preservation.

Irrigation as a biomimetic of blood flow—Simulations predicted that irrigation of electrode-apposed tissue with room-temperature saline discharged at the convective rate of luminal blood protects the intima and media from excessive injury (Fig 5A,B vs Fig 3C,D), without appreciably altering peri-arterial ablation geometry. This is highlighted in images of simulated wall injury which show greater media preservation when the rate of irrigation is doubled (Fig 6 A–C). When an RF treatment was directed at an HCAS such as lymph node, irrigation was predicted to efficiently protect only the immediate tissue surroundings of the electrode (Fig 5Ai). When HCAS are all lateral to the electrode, the protective effects of irrigation extend beyond the mural interface to most of the arterial media (Fig 5B,Bi vs Fig 3D). The resulting wall injury patterns in the presence of irrigation are therefore localized to small islands that are disconnected from the lumen and track the orientation of the surrounding HCAS (Fig 6D–F). In certain cases, this can create the misleading impression that two ablation sites were observed in the histologic cross sections when only one treatment was administered.

Irrigated discrete electrode treatments—We validated the predicted effects of electrode irrigation in animal models in which we applied discrete- and five-electrode catheter-based RF RDN. The discrete electrode experiments allowed a detailed comparison of the results to the predictions of our model. The five-electrode treatment represents the clinically relevant protocol.

We treated 3 arteries with irrigated discrete RF electrodes and then assessed tissue damage after 7 days. Whereas non irrigated, discrete treatments injured the intima and media surroundings of the electrode in a well-defined luminal arc (e.g. Fig 1C–G and especially Gi), irrigated discrete treatments spared contiguous regions of the intima and inner media near the electrode (Fig 7Ai, Bi) Consistent with model simulations (e.g. Fig 6A,D vs 6B,E or 6C,F), partial sparing of adluminal arterial media was achieved without qualitatively affecting the extent of peri-arterial effects (Fig 7Ai,Bi, Table 1). Quantitative morphometry performed on maximal injury zones confirmed that irrigation lowered the affected luminal circumference (13.7±19.1% vs 40.1±6.7%, P=0.082), affected circumference at the EEL (27.0±19.8% vs 43.4±5.5%, P=0.126), affected media area (16.7±16.9% vs 36.1±6.6%, P=0.126), and media thinning (25.7±22.6% vs 37.3±19.5%, P=0.383) (Fig 1 C–G). The average ablation area, depth and width, percentage of affected nerves (Table 1), and NEPI (536.7± 27.4 ng/g, 3 kidneys, 2 samples each) were statistically equivalent, indicating that the overall effect was unchanged by irrigation.

Clinically relevant five-electrode irrigated treatments

When the effect of irrigation was tested in animals treated with the concomitant five RF electrodes the surrounding tissue was invariably injured, which appeared as contiguous areas of coagulative necrosis. Endothelialization was nearly complete with negligible to minimal neointima and no luminal occlusion (Fig 8A,B). Quantitative morphometry of the maximal zones of injury revealed necrosis across 21.7±22.8% of the luminal circumference and 23.5±15.5% of media area. Mural necrosis led to wall thinning of up to 54.5% (37.0±19.6%). Taken together, these results illustrate that the media-preserving benefits of electrode irrigation extend to the multi-electrode setting, although to a slightly lesser degree, presumably a result of cross effects of neighboring RF electrodes.

Peri-arterial damage accounted for more than 96% of the maximal ablation zone areas. Maximal ablation zones (Fig 8C–F) varied in orientation, shape, area (33.7±18.1 mm2), width (7.8±1.8 mm), and depth (4.4±1.0 mm) and often included or bordered lymph nodes, large blood vessels and the hypaxial skeletal muscle. In line with our model'spredictions, the presence of blood vessels near the treatment site (Fig 8 C–D) coincided with preservation of those tissues regions and limited ablation from spreading beyond them. In total, 74±10% of nerves were affected in sections with maximal ablation zones. Approximately half (51±7%) of the affected nerves were located within the maximal ablation zone. Half (54±22%) of nerves outside the traced ablation zones were also affected. Ablation resulted in kidney NEPI concentrations between 0–359 ng/g (68.8±111.4 ng/g, 8 kidneys, 2 samples each), significantly below the baseline range of untreated controls 649±161 ng/g(19). Taken together, these data illustrate that the wall-protective effects of irrigation can coincide with significant peri-arterial ablation and NEPI reduction.

To examine how treatment with the five-electrode irrigated catheters affected BP, we applied the same irrigated RF catheter procedure unilaterally to a different group of 10 normotensive Yucatan swine. Treatment reduced systolic BP (SBP) by 25.7 mmHg (P=0.004) and mean arterial pressure (MAP) by 16.2 mmHg (P=0.024). Overall, SBP was reduced in 8 of the 10 treated animals (Table S2), and in these animals, the percent changes in BP correlated with the size-weighted number of non-lethally injured (degenerative) nerves in maximally affected tissue sections (Fig. 9). Thus, the degree of BP reduction 7 days after RDN was determined by the fraction of nerves that are exposed to RF treatments near each of the 5 electrodes, their sizes, and the degree to which they are affected.

DISCUSSION

RDN effectively lowers BP in certain but not in all patients (5–6) raising speculation (8–9) as to heterogeneous mechanisms of hypertension, suboptimal nerve ablation by the current technology/device design, and limits to procedural implementation related to power or positioning of single electrode catheters (9, 17). Indeed, retrospective analysis of stored angiographic and procedural records of all RF energy applications of the SYMPLICITY HTN-3 Trial data revealed (21) that only 84% of ablation attempts resulted in 120 sec long ablations as recommended, and that only 6% of all patients received bilateral, fully circumferential ablations, as recommended in the trial protocol. Moreover, due to the asymmetric innervation of renal arteries (12) and, in lieu of technologies that assess nerve

distribution peri-procedurally, controlled catheter positioning and power do not guarantee that ablation areas encompass target nerves (13, 22). The current study illustrates that the distribution of RF energy at the delivery site is largely dictated by local anatomic features of the treated tissue. Given our finding that BP linearly tracks with the number of degenerative nerves in maximal ablation zones, the efficacy of RDN would seem to depend not only on the nerve abundance near the multiple treatments sites, but also on the latter's anatomic milieu.

The role of electric conductivity and heat sink gradients

The complexity of RDN has likely been under-appreciated, in part as the intricacy of the renal environment (with variation in venous and arterial perfusion, nerve and ganglia distribution, lymph nodes, etc.) stands in contrast to the simple functional and structural anatomy of the myocardium. Extrapolating from cardiac ablation to RDN is not appropriate.

Ablation in RDN rarely occurs in a homogenous soft tissue (Figs 1, 8). Rather, it typically includes regional structures such as lymph nodes, large veins and arteries, and hypaxial skeletal muscle with fibrous sheaths. When applied caudally, even the ureter can be involved (Fig 8E). Electrical conductivity varies considerably among tissues on the basis of their water and fat content. Our computational modeling illustrates that the resulting electric conductivity gradients can facilitate peri-arterial power delivery or limit its distribution. For example, the conductivity gradient across the EEL helps to direct RF power to the nerve-rich aspect of the EEL, as this gradient relies on the naturally layered structure of the arterial wall in animals and humans. By contrast, peri-arterial conductivity gradients are unpredictable, a result of high micro-anatomic variability. Fibrous sheaths and skeletal muscles are generally located dorsally and ureters caudally, but lymph nodes and vascular structures reside at variable distances from the renal artery wall and at variable orientations.

Computational simulations revealed the influence of the orientation of HCAS and blood vessels (HCAS/HS) relative to the electrode. When laterally oriented relative to the electrode, peri-arterial tissues drew power from the electrode and increased the arc and area of ablation area without substantially affecting maximal ablation depth distal to the electrode-tissue interface (Fig 4A & Fig 3B–D vs Fig 2E), thereby increasing the probability of damaging peri-arterial nerves. In contrast, when the electrode is directed at nearby HCAS, e.g. when they are located between the electrode and the location at which peak temperature would have been achieved in their absence, ablation depth is reduced but circumferential spread is only minimally affected (Fig 2E vs Fig 3A). The effects of peri-arterial blood vessels (HCAS/HS) are even more dramatic, as these efficiently dissipate surrounding heat. The net result of an ablation targeted directly (Fig 4D) or even laterally at large HCAS or HS (Fig 4E–H) is a large reduction in maximal ablation depth and shielding of the surrounding nerves from the intended treatment. Thus the micro-anatomy local to each individual's treatment site may play a role in determining their response to the treatment and therefore the overall percentage of clinical non-responders in RDN therapies.

Although in our experience large veins were most commonly found in the anterior quadrant, this was not always the case (e.g. Fig 1D) and neighboring arteries could be found in other quadrants. In lieu of technologies to identify the locations of periadventital vessels and guide

treatments away from such heat sinks, clinical efficacy should be optimized by the application of multiple, circumferentially staggered treatments along the target artery.

Irrigation as a biomimetic of blood flow

Prior to the introduction of irrigated RF catheters for the treatment of cardiac arrhythmias, clinical efficacy was limited by coagulum formation and impedance rise at relatively low power levels and durations (7W/30 sec), a result of limited convective cooling by circulating endocavitary blood (23–24). Because myocardial tissue is relatively homogenous, peak temperature in the tissue is achieved in the electrode contacting areas (20), and electrode irrigation can concomitantly reduce coagulum formation and tissue damage (25–26) while treating at high powers (30–50W). Yet, some have questioned the utility of RF electrode irrigation for RDN, suggesting that the greater blood flow in renal arteries should efficiently clear excess heat from luminal electrodes (27).

However, our histomorphometric evaluation of RDN-treated pigs illustrated that arterial blood flow alone is not an efficient heat sink in the vicinity of mural electrodes (Fig 1 C–G) and that electrode irrigation can protect the arterial wall, particularly the adluminal regions, from thermal injury (Fig 7 Aii,Bii). Although the protected adluminal area is not large, the physiologic effect can be profound given the sensitivity of the endothelial layer and the inner media to vascular injury. As shown by OCT in animals (15) and humans (16), such vascular injuries may not be apparent in angiography and can potentially lead to acute thrombosis and subacute fibrosis and inflammation.

Computational modeling explains RF power distribution peaks inside the tissue and shows that diffusing heat is efficiently cleared by blood flow around the electrode; electrode-apposed tissue is shielded from blood flow, so tissue close to the electrode is particularly prone to injury. Owing to its lower temperature and more radial flow lines, saline irrigation through electrode ports can greatly enhance the cooling effects of blood without substantially reducing peri-arterial temperatures (Fig 6). These simulation results, along with our quantification of ablation areas, percent affected nerves and NEPI data suggest that irrigation can alleviate the concern for mural thrombus formation, while ablating the nerve-rich adventitia to the same degree as non-irrigated treatments. Whereas our experimental findings were based on discrete electrode treatments, Sakaural *et al*. (28) reported consistent findings in pig arteries that were treated with the same catheter and power settings, but stimulating all 5 electrodes. Irrigation lowered media thinning and injured media circumference while slightly reducing ablation depth at equivalent nerve injury and NEPI. Moreover RDN of hypertensive dogs with an irrigated RF catheter reduces BP without ablation-related complications one and three months after the procedure (29). Small clinical studies have also shown BP reductions without complications after RDN with irrigated RF catheters (30–31), but these results require follow up in larger cohorts.

Does blood pressure reduction require threshold nerve ablation?

Understanding the relationship between systemic markers of RDN efficacy as reported in clinical studies (BP, NEPI spillover) and local nerve ablation, currently only measured in preclinical studies, is key to successful translation of this therapy. Preclinical studies that

report BP, NEPI and nerve effects can provide important insights, but are rare due to technical complexity and cost. Previously, Henegar *et al*. reported that (32) BP reduction in hypertensive, obese dogs 8 weeks after bilateral RDN, was associated with a 42% reduction renal NEPI concentrations and injury to 46% of counted nerves. Esler recently highlighted the similarity between these estimates of denervation in dogs to the clinical reduction in norepinephrine spillover from renal sympathetic nerves to plasma after RDN in HTN-1, 40–47% (4, 17). Thus, both human and animal data suggest that significant BP reduction does not require complete nerve ablation. Herein, we found that unilateral RDN of Yucatan swine significantly reduced BP. Moreover the percent reductions in 8 of the 10 treated swine increased linearly with the size-weighted number of non-lethally injured (degenerative) nerves in maximally affected tissue sections (Fig. 9). The smooth dependence of BP reduction on the number of degenerative nerves contrasts with the sharp, threshold-like dependence of renal NEPI levels on the fraction of affected nerves (13, 33), degenerative or necrotic, suggesting that BP is not solely determined by NEPI concentration. Thus, although NEPI tracks with histologically apparent sympathetic denervation (13, 33), BP may be sensitive to particular types of nerve disruptions or changes in afferent signaling. Indeed, recently published data (34) show that reductions in BP after RDN in patients with drug-resistant hypertension did not correlate tightly with sympathetic activity, as measured by single fiber nerve firing rates.

Limitations

The current study used ablation geometry, histopathological assessments of nerve effects and bioanalytical quantification of renal NEPI levels as surrogate markers for sympathetic denervation and nerve firing. Although our histological methods did not differentiate between afferent and efferent nerves, we (13) and others (12, 14) have shown with specific stains that efferent and afferent nerve fibers are intermixed and that the former overwhelmingly outnumber the latter. The finding that BP reduction in unilaterally denervated pigs correlates linearly with the total number of degenerative nerves in maximally treated sections, contrasts with the threshold dependence of NEPI on the total percent of affected nerves by histology and may imply that BP reductions were partly due to disruption of afferent signaling.

Ideally, BP measurements should be taken in conscious animals under controlled environmental conditions that minimize stress. Our use of intra-arterial pressure transducers to monitor BP under anesthesia could be problematic because variations in stress levels and anesthesia may have confounded BP readouts.

Finally, while histology micrographs and two dimensional computational models provide insight into the mechanistic determinants of ablation geometries, they cannot account for out of plane anatomic structures or electrodes, limiting our ability to account for some of the histologically observed ablation patterns. Indeed, the counterintuitive finding that a large fraction of affected nerves after multielectrode treatments do not reside in observed ablation zones suggests that the resposible ablation zones appear in neighboring sections.

CONCLUSION

Our data inform the discussion regarding the predictably, variability and treatment success of catheter-based RDN. The effects of application of focal energy fields to perivascular nerves and ganglia cannot be determined without knowing the architecture of the local tissue. Every element in the tissue contributes to the focusing of applied energy and dissipation or conduction of heat. Further, patients treated with RDN often have atherosclerotic and hyperplastic vessels whose microanatomy is even more complex than the intact healthy normotensive pig vessels that we examined. Treatment designs that do not take these factors into account cannot provide optimal alternatives to the first generation RDN systems and may be plagued by variable effects. In lieu of technologies that assess nerve distribution and location of neighboring blood vessels, catheter-based ablation efficacy might be optimized through the application of multiple electrode treatments along the circumference of the renal artery.

METHODS

Experimental design

The reported animal studies were originally designed to correlate ablation zone geometry with the anatomy of the treatment site and to assess the ability of arterial blood flow to protect the mural treatment sites. Preliminary review of histology suggested that ablation patterns correlated with local microanatomy and that cooling by blood could not adequately preserve arterial tissue in the electrodes vicinity. As there is no way to control target microanatomy, a computational model was developed to provide supporting insight into experimental data. Intraprocedural BP measurements were not included in the original study design, but are reported for a different group of unilaterally treated swine assessed subsequently. Minimum sample sizes were calculated for 80% power and a P value of less than 0.05 based on SBP and NEPI reduction endpoints described below.

Animal Model

All animal experiments were performed at CBSET, Inc. (AAALAC accredited) in accordance with federal USDA and institutional IACUC oversight. Male (castrated) or female (nulliparous) Yorkshire swine (n=7), between 40.4–78.2 kg, underwent percutaneous bilateral RDN. An additional 10 Yucatan swine (5 castrated male and 5 nulliparous female), between 33.8 and 42.7 kg, underwent percutaneous unilateral RDN in the right renal artery.

Bilateral and unilateral RF treatments with controlled irrigation were performed at up to 5 longitudinally staggered discrete locations using a RenLane Renal Denervation catheter. A multi-channel generator controlled the power of each electrode (based on pre-specified power and temperature set points) and the irrigation rate of room temperature saline (~23°C) through ports along each of the electrodes. To reduce variability in energy delivery by monopolar electrodes, ground pads were placed at the same position (between the shoulder blades) in each treated animal. In three Yorkshire swine (Group 1), each artery was treated by 2–3 non-neighboring electrodes (15W/30 sec) that were either irrigated at a rate of 30 ml/sec (3 arteries) or non-irrigated (3 arteries). Four Yorkshire swine (Group 2) underwent

bilateral treatment by all five electrodes (15W/30 sec) with irrigation (30 ml/sec). Ten Yucatan swine (Group 3) underwent unilateral treatment by all five electrodes (9–10W/30 sec) with irrigation (30 ml/sec). Temperature set points were 50°C for all irrigated treatments and 65°C for non-irrigated treatments. Impedance and temperature were monitored during RF application for each electrode. Angiographic vessel diameters for Groups 1 and 2 treatments ranged from 5.04–5.99 mm for all but one of the treatments (in Group 1, one caudal arterial segment of 3.45 mm diameter was treated by an irrigated electrode) and from 4.13–4.95 mm for Group 3.

Tissue collection and kidney bioanalysis

All animals were euthanized at day 7. Renal arteries and associated tissue were removed, perfused with 10% Neutral Buffered Formalin (NBF), immersed in 10% NBF and processed for histology. Both kidneys were collected, flash frozen in dry ice or liquid nitrogen and stored at approximately -80°C. Two ~4 g renal aliquots were homogenized and analyzed for NEPI by LC/MS/MS(19). Using these methods, we have previously shown that NEPI levels in untreated animals(19) are 649±161 ng/g (70 kidneys). On the basis of a 50% NEPI reduction endpoint, 2 arteries/kidneys are required provide 80% power, with the use of a two-sided significance level of 0.05.

Histology of renal arteries

Each treated renal artery with surrounding tissue was trimmed every 3–5 mm to yield at least three cross-sections for paraffin-embedding. One hematoxylin and eosin-stained slide and one Masson's elastin Trichrome-stained slide was generated per section.

Histopathology evaluation and nerve assessment

Histologic sections were examined under light microscopy by board-certified veterinary pathologists with extensive experience in the RDN model to evaluate the tissue response to treatment. Tissue ablation was evaluated qualitatively, and quantified using Olympus MicroSuite Biological Suite. Metrics included: (1) total treatment area, depth and width; (2) percent luminal surface, EEL, and medial area affected; and (3) medial thickness. Nerves and ganglia were counted, their status with regard to treatment zone determined, and any nerve changes characterized as degenerative (sublethal injuries), necrotic, or chronic/reactive(13, 19). In unilaterally treated animals, counted nerves were also scored for size d (s=1 for d <0.5 mm, s=3 for 0.5<d<1.0 mm, and s= 5 for 1.0<d<1.5 mm).

Blood pressure measurements and correlation with nerve injury after unilateral treatments

A Meritrans pressure transducer (Merit Medical Systems) was placed in the left femoral artery prior to the unilateral denervation procedure. Mean arterial BP, MAP, was estimated as the algebraic sum of the time averaged systolic (SBP) and diastolic (DBP) BP readouts

$$MAP = \frac{1}{3} \cdot (SBP + 2 \cdot DBP). \quad [1]$$

The normalized percent change in pre (0d) and post (7d) pressures were evaluated for each animal as

$$\Delta SBP = 100 \cdot \frac{SBP(7d) - SBP(0)}{SBP(0)} \quad [2]$$

and

$$\Delta MAP = 100 \cdot \frac{MAP(7d) - MAP(0)}{MAP(0)} \quad [3]$$

and correlated with the total number of injured nerves per artery with Microsoft Excel. Statistically significant regression results were obtained when sublethal injured nerve counts (*ni*) in each artery were weighted according to their respective size score (*si*) to obtain the size weighted number of degenerative nerves per artery

$$N_{artery} = \sum_i s_i n_i. \quad [4]$$

On the basis of a 25 mm Hg SBP reduction endpoint, 5 unilateral treatments are required provide 80% power, with the use of a two-sided significance level of 0.05.

Data analysis and statistics

Experimental values are reported as mean ± standard deviation. For selected continuous data, if the assumptions of normality and homogeneity of variance were met, treatment differences were assessed by group t-test. If normality or homogeneity of variance were not met, treatment differences were assessed by Mann–Whitney Rank Sum test. For all statistical tests, the null hypothesis of no difference was only rejected if the value of the calculated statistic was less than 0.05 ($p<0.05$).

Computational modeling

In our in vivo studies, ablation electrodes operated at radiofrequencies of 480 kHz (±3%), ensuring that current is predominantly resistive and electrode dimensions are negligible relative to the electromagnetic wavelength (35). Consequently, RF power density in the tissue is determined by the static electric conductivities of the affected tissues σ and their quasi-static electric potential ϕ as $\sigma|\nabla\varphi|^2$ where ∇ is the gradient operator. This Joule heating term is calculated by solving Laplace's equation

$$\nabla \cdot [\sigma \nabla \phi] = 0 \quad [5]$$

and represents a source in a heat diffusion equation

$$\underbrace{\rho C}_{\substack{\text{heat} \\ \text{capacitance}}} \frac{\partial T}{\partial t} - \underbrace{\nabla \cdot [\kappa \nabla T]}_{\text{heat diffusion}} = \underbrace{\sigma |\nabla \phi|^2}_{\text{RF power density}} \quad [6]$$

where *T*, ρ, *C*, and κ are, respectively, the local tissue temperature, density, heat capacity and thermal conductivity(36). At onset (*t*=0), electric potential and temperature were set to ambient body values (ϕ=0 and *T*=37°C). These conditions were assumed to persist at the periphery of the computational domain. At blood-tissue interfaces, electric potential was

determined by enforcing current ($\sigma\nabla\varphi$) continuity whereas temperature was determined by a linear cooling law(36)

$$k\nabla_n T = h_{blood}(T_{blood} - T). \quad [7]$$

Here ∇_n is the normal component of the gradient operator, T_{blood} = 37°C is the ambient blood temperature, and $h_{blood} = 3\times10^5$ erg·s^{-1}·cm^{-2}·C^{-1} is the convective heat transfer coefficient of blood. At the electrode-tissue interface potential was prescribed a constant value V_s, (33 Volts) while temperature was calculated based on a linear heat exchange law

$$\kappa\,\nabla_n T = h_s(T_s - T). \quad [8]$$

Irrigated treatments were modeled using the estimates $h_s = 2.5\times10^5$ erg·s^{-1}·cm^{-2}·C^{-1} and T_s = 23°C for the irrigant. Non-irrigated ablations were modeled by setting h_s=0. Local thermal injury was assumed to be confined to tissue regions with time averaged temperature in excess of 43.5°C, the temperature at which the activation energy of thermal injury to human cell survival abruptly changes as reflected by a breakpoint in the slope of Arrhenius plots(37).

Equations 5–8 were solved numerically in a 2.7×2.7 cm2 computational domain using the finite element package COMSOL 3.5 as described in detail in the S**upplementary Materials**. Electrode and artery cross-sections were modeled as perfectly circular with radii of 1 mm and 3 mm, respectively. Electrode apposition was assumed to slightly deform adjacent arterial tissue, and modeled as 100 μm embedding. The tissue was comprised of a 1mm thick ring of arterial media surrounded by peri-arterial tissue with fat–like transport properties interspersed with high conductivity lymph nodes and blood vessels. Lymph nodes were modeled as solid circles (2.5 mm radius), while peri-arterial blood vessels were modeled as circles and ellipses and that clear heat based on the local temperature gradient at their wall (Eq. 7). The values of the electric and thermal constants for blood and tissue compartments were based on published estimates (Table S1). Note that the finite element formulation naturally ensures continuity of electric current across boundaries of electric conductivity discontinuity.

Supplementary Material

Refer to Web version on PubMed Central for supplementary material.

Acknowledgments

Funding: This study was supported in part by National Institutes of Health grant (R01 GM-49039) to EE and research grants from Cordis/Biosense Webster, Inc. a Johnson & Johnson Company to CBSET.

DG, PO, and KF are employees of Cordis/Biosense Webster, Inc. a Johnson & Johnson Company. Biosense Webster owns patents related to the design of the catheter. FM was investigator of SYMPLICITY HTN-1 and HTN-2 trial. FM received research grants, speaker honorarium and/or consultancy fees from Medtronic/Ardian, St. Jude, Boston Scientific, and/or Cordis and is supported by Deutsche Hochdruckliga and Deutsche Gesellschaft für Kardiologie.

References

1. Esler M. The sympathetic system and hypertension. Am J Hypertens. 2000; 13:99S–105S. [PubMed: 10921528]
2. Hausberg M, Kosch M, Harmelink P, Barenbrock M, Hohage H, Kisters K, Dietl KH, Rahn KH. Sympathetic nerve activity in end-stage renal disease. Circulation. 2002; 106:1974–1979. [PubMed: 12370222]
3. Smithwick RH, Thompson JE. Splanchnicectomy for essential hypertension; results in 1,266 cases. J Am Med Assoc. 1953; 152:1501–1504. [PubMed: 13061307]
4. Krum H, Schlaich M, Whitbourn R, Sobotka PA, Sadowski J, Bartus K, Kapelak B, Walton A, Sievert H, Thambar S, Abraham WT, Esler M. Catheter-based renal sympathetic denervation for resistant hypertension: a multicentre safety and proof-of-principle cohort study. Lancet. 2009; 373:1275–1281. [PubMed: 19332353]
5. Symplicity HTN-1 Investigators. Catheter-based renal sympathetic denervation for resistant hypertension: durability of blood pressure reduction out to 24 months. Hypertension. 2011; 57:911–917. [PubMed: 21403086]
6. Esler MD, Krum H, Schlaich M, Schmieder RE, Bohm M, Sobotka PA. Renal sympathetic denervation for treatment of drug-resistant hypertension: one-year results from the Symplicity HTN-2 randomized, controlled trial. Circulation. 2012; 126:2976–2982. [PubMed: 23248063]
7. Krum H, Sobotka P, Schlaich M, Bohm M, Esler M. Renal denervation for resistant hypertension-the Symplicity HTN-1 study – Authors' reply. Lancet. 2014; 383:1885–1886. [PubMed: 24881987]
8. Tsioufis C, Mahfoud F, Mancia G, Redon J, Damascelli B, Zeller T, Schmieder RE. What the interventionalist should know about renal denervation in hypertensive patients: a position paper by the ESH WG on the interventional treatment of hypertension. EuroIntervention. 2014; 9:1027–1035. [PubMed: 24457275]
9. Ukena C, Cremers B, Ewen S, Bohm M, Mahfoud F. Response and non-response to renal denervation: who is the ideal candidate? EuroIntervention. 2013; 9(Suppl R):R54–57. [PubMed: 23732156]
10. Bhatt DL, Kandzari DE, O'Neill WW, D'Agostino R, Flack JM, Katzen BT, Leon MB, Liu M, Mauri L, Negoita M, Cohen SA, Oparil S, Rocha-Singh K, Townsend RR, Bakris GL. A Controlled Trial of Renal Denervation for Resistant Hypertension. N Engl J Med. 2014
11. Papademetriou V, Rashidi AA, Tsioufis C, Doumas M. Renal nerve ablation for resistant hypertension: how did we get here, present status, and future directions. Circulation. 2014; 129:1440–1451. [PubMed: 24687645]
12. Sakakura K, Ladich E, Cheng Q, Otsuka F, Yahagi K, Fowler DR, Kolodgie FD, Virmani R, Joner M. Anatomic assessment of sympathetic peri-arterial renal nerves in man. J Am Coll Cardiol. 2014; 64:635–643. [PubMed: 25125292]
13. Tzafriri AR, Mahfoud F, Keating JH, Markham PM, Spognardi A, Wong G, Fuimaono K, Böhm M, Edelman ER. Innervation patterns may limit response to endovascular renal denervation. JACC. 2014; 64:1079–1087. [PubMed: 25212640]
14. Tellez A, Rousselle S, Palmieri T, Rate WRt, Wicks J, Degrange A, Hyon CM, Gongora CA, Hart R, Grundy W, Kaluza GL, Granada JF. Renal artery nerve distribution and density in the porcine model: biologic implications for the development of radiofrequency ablation therapies. Transl Res. 2013; 162:381–389. [PubMed: 23911638]
15. Steigerwald K, Titova A, Malle C, Kennerknecht E, Jilek C, Hausleiter J, Nahrig JM, Laugwitz KL, Joner M. Morphological assessment of renal arteries after radiofrequency catheter-based sympathetic denervation in a porcine model. J Hypertens. 2012; 30:2230–2239. [PubMed: 22914572]
16. Templin C, Jaguszewski M, Ghadri JR, Sudano I, Gaehwiler R, Hellermann JP, Schoenenberger-Berzins R, Landmesser U, Erne P, Noll G, Luscher TF. Vascular lesions induced by renal nerve ablation as assessed by optical coherence tomography: pre- and post-procedural comparison with the Simplicity catheter system and the EnligHTN multi-electrode renal denervation catheter. Eur Heart J. 2013; 34:2141–2148. 2148b. [PubMed: 23620498]

17. Esler M. Illusions of truths in the Symplicity HTN-3 trial: generic design strengths but neuroscience failings. J Am Soc Hypertens. 2014; 8:593–598. [PubMed: 25151320]
18. Vink EE, Goldschmeding R, Vink A, Weggemans C, Bleijs RL, Blankestijn PJ. Limited destruction of renal nerves after catheter-based renal denervation: results of a human case study. Nephrol Dial Transplant. 2014; 29:1608–1610. [PubMed: 24875664]
19. Sakakura K, Ladich E, Edelman ER, Markham PM, Stanley JRL, Keating J, Kolodgie FD, Virmani R, Joner M. Methodological standardization for the preclinical evaluation of renal sympathetic denervation. JACC Cardiovasc Interv. 2014; 7:1184–1193. [PubMed: 25240550]
20. Haines DE, Watson DD. Tissue heating during radiofrequency catheter ablation: a thermodynamic model and observations in isolated perfused and superfused canine right ventricular free wall. Pacing Clin Electrophysiol. 1989; 12:962–976. [PubMed: 2472624]
21. Kandzari DE, Bhatt DL, Brar S, Devireddy CM, Esler M, Fahy M, Flack JM, Katzen BT, Lea J, Lee DP, Leon MB, Ma A, Massaro J, Mauri L, Oparil S, O'Neill WW, Patel MR, Rocha-Singh K, Sobotka PA, Svetkey L, Townsend RR, Bakris GL. Predictors of blood pressure response in the SYMPLICITY HTN-3 trial. Eur Heart J. 2015; 36:219–227. [PubMed: 25400162]
22. Vink EE, de Beus E, de Jager RL, Voskuil M, Spiering W, Vonken EJ, de Wit GA, Roes KC, Bots ML, Blankestijn PJ. The effect of renal denervation added to standard pharmacologic treatment versus standard pharmacologic treatment alone in patients with resistant hypertension: rationale and design of the SYMPATHY trial. Am Heart J. 2014; 167:308–314 e303. [PubMed: 24576513]
23. Wittkampf FH, Hauer RN, Robles de Medina EO. Control of radiofrequency lesion size by power regulation. Circulation. 1989; 80:962–968. [PubMed: 2791254]
24. Schwartzman D, Michele JJ, Trankiem CT, Ren JF. Electrogram-guided radiofrequency catheter ablation of atrial tissue comparison with thermometry-guide ablation. J Interv Card Electrophysiol. 2001; 5:253–266. [PubMed: 11500580]
25. Nakagawa H, Yamanashi WS, Pitha JV, Arruda M, Wang X, Ohtomo K, Beckman KJ, McClelland JH, Lazzara R, Jackman WM. Comparison of in vivo tissue temperature profile and lesion geometry for radiofrequency ablation with a saline-irrigated electrode versus temperature control in a canine thigh muscle preparation. Circulation. 1995; 91:2264–2273. [PubMed: 7697856]
26. Vest JA, Seiler J, Stevenson WG. Clinical use of cooled radiofrequency ablation. J Cardiovasc Electrophysiol. 2008; 19:769–773. [PubMed: 18479328]
27. Blessing E, Esler MD, Francis DP, Schmieder RE. Cardiac ablation and renal denervation systems have distinct purposes and different technical requirements. JACC Cardiovasc Interv. 2012; 6:314. [PubMed: 23517846]
28. Sakakura K, Ladich E, Fuimaono K, Grunewald D, O'Fallon P, Spognardi AM, Markham P, Otsuka F, Yahagi K, Shen K, Kolodgie FD, Joner M, Virmani R. Comparison of renal artery, soft tissue, and nerve damage after irrigated versus nonirrigated radiofrequency ablation. Circ Cardiovasc Interv. 10.1161/CIRCINTERVENTIONS.114.001720
29. Lu J, Ling Z, Chen W, Du H, Xu Y, Fan J, Long Y, Chen S, Xiao P, Liu Z, Zrenner B, Yin Y. Effects of renal sympathetic denervation using saline-irrigated radiofrequency ablation catheter on the activity of the renin-angiotensin system and endothelin-1. Journal of Renin-Angiotensin-Aldosterone System. 2014; 15:532–539.
30. Ahmed H, Neuzil P, Skoda J, Petru J, Sediva L, Schejbalova M, Reddy VY. Renal sympathetic denervation using an irrigated radiofrequency ablation catheter for the management of drug-resistant hypertension. JACC Cardiovasc Interv. 2012; 5:758–765. [PubMed: 22814781]
31. Armaganijan L, Staico R, Moraes A, Abizaid A, Moreira D, Amodeo C, Sousa M, Borelli F, Armaganijan D, Sousa JE, Sousa A. Renal Denervation Using an Irrigated Catheter in Patients with Resistant Hypertension: A Promising Strategy? Arq Bras Cardiol. 2014; 102:355–363. [PubMed: 24652055]
32. Henegar JR, Zhang Y, Rama RD, Hata C, Hall ME, Hall JE. Catheter-Based Radiorefrequency Renal Denervation Lowers Blood Pressure in Obese Hypertensive Dogs. Am J Hypertens. 2014
33. Tzafriri AR, Mahfoud F, Keating J, Wong G, Spognardi A, Stanley JRL, Highsmith D, O'Fallon P, Edelman ER. TCT-402 Renal Norepinephrine Reduction Following Radiofrequency Renal Denervation Correlates with Extent of Nerve Ablation: Roles of Ablation Areas, Anatomy, and Number of Treatments. JACC. 2014; 64:B119.

34. Esler M. Renal denervation for hypertension: observations and predictions of a founder. Eur Heart J. 2014; 35:1178–1185. [PubMed: 24598982]
35. Doss JD. Calculation of electric fields in conductive media. Med Phys. 1982; 9:566–573. [PubMed: 7110088]
36. Cao H, Vorperian VR, Tungjitkusolmun S, Tsai JZ, Haemmerich D, Choy YB, Webster JG. Flow effect on lesion formation in RF cardiac catheter ablation. IEEE Trans Biomed Eng. 2001; 48:425–433. [PubMed: 11322530]
37. Dewhirst MW, Viglianti BL, Lora-Michiels M, Hanson M, Hoopes PJ. Basic principles of thermal dosimetry and thermal thresholds for tissue damage from hyperthermia. Int J Hyperthermia. 2003; 19:267–294. [PubMed: 12745972]
38. Edgerton RH. Radial conductivity of arterial walls. Med Biol Eng. 1975; 13:531–534. [PubMed: 1238883]
39. Ley O, Kim T. Calculation of arterial wall temperature in atherosclerotic arteries: effect of pulsatile flow, arterial geometry, and plaque structure. Biomed Eng Online. 2007; 6:8. [PubMed: 17331253]
40. Anderson V, McIntosh RL. A comprehensive tissue properties database provided for the thermal assessment of a human at rest. Biophysical Reviews and Letters. 2010; 05:129–151.
41. Gabriel C, Peyman A, Grant EH. Electrical conductivity of tissue at frequencies below 1 MHz. Phys Med Biol. 2009; 54:4863–4878. [PubMed: 19636081]
42. Hasgall PA, Neufeld E, Gosselin MC, Klingenböck A, Kuster N. 2013
43. Rivera MJ, Lopez Molina JA, Trujillo M, Romero-Garcia V, Berjano EJ. Analytical validation of COMSOL Multiphysics for theoretical models of Radiofrequency ablation including the Hyperbolic Bioheat transfer equation. Conf Proc IEEE Eng Med Biol Soc. 2010:3214–3217. [PubMed: 21096815]
44. Haemmerich D, Chachati L, Wright AS, Mahvi DM, Lee FT Jr, Webster JG. Hepatic radiofrequency ablation with internally cooled probes: effect of coolant temperature on lesion size. IEEE Trans Biomed Eng. 2003; 50:493–500. [PubMed: 12723061]

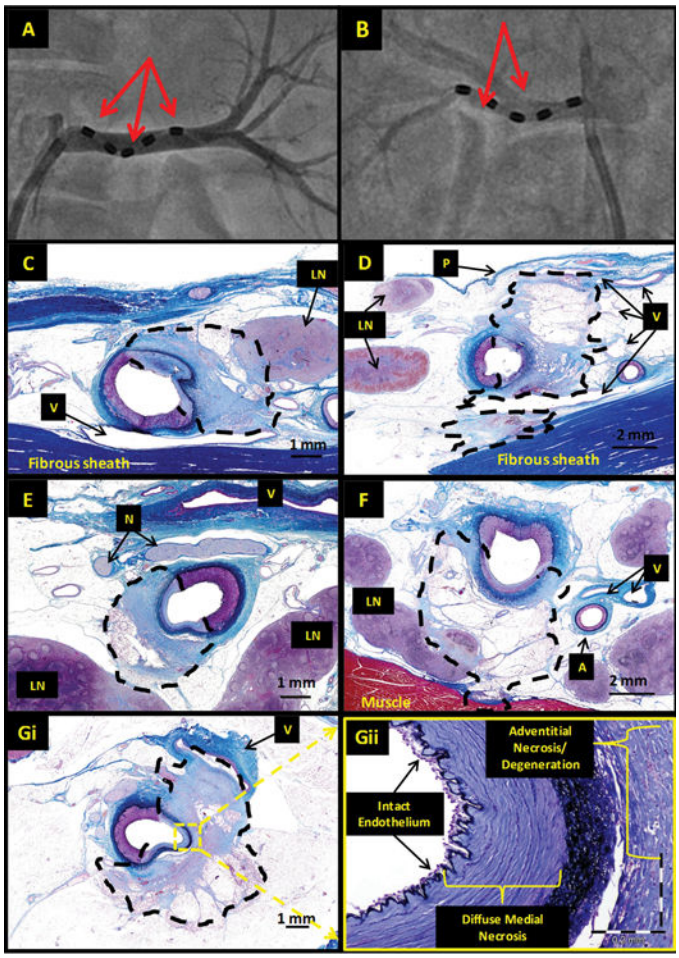

Figure 1. Arterial and peri-arterial sympathetic ablation by non-irrigated discrete RF electrodes (A and B). Locations (arrows) of non-irrigated electrode treatments by angiography in the right arteries of two pigs (out of a total of 3 Yorkshire swine arteries treated without irrigation). (C through G) Micrographs of Masson's trichrome stained sections with overlaid maximal ablation zones (dashed lines) for each of the treatments sites in arteries shown in A (C, E, G) and B (D, F), starting with the treatment area closest to the aorta. The locations of the EEL and tunica media (TM) are denoted (arrows) in (C). (Gii) A higher magnification view of the yellow rectangular area depicted in (Gi) demonstrating necrosis (blue stain) extending through the arterial media and into surrounding adventitia. A=artery, LN=lymph node, N=nerve, P=peritoneum, V=vessel.

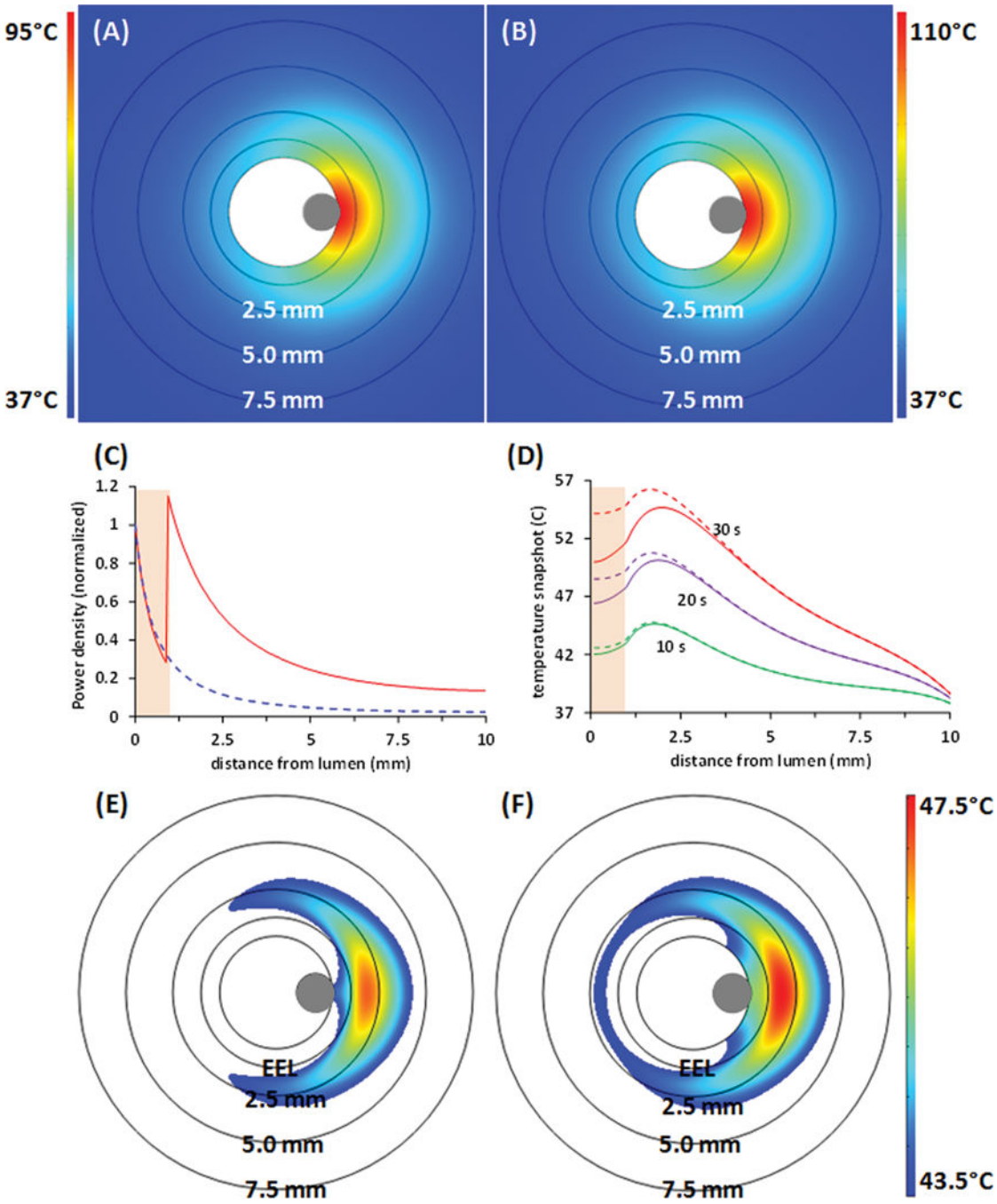

Figure 2. Model-predicted temperature and injury patterns for non-irrigated single-electrode RF treatments of homogeneous or layered tissues

Temperature maps at 30 sec after an RF stimulus are depicted for a homogeneous tissue with media-like (A) or fat-like (B) electric and thermal properties. Temperature-color scales are provided to the right of each panel. The first ring in the tissue denotes the location of the EEL (1mm from the lumen), and subsequent rings mark distance from the lumen. (C) Power distribution for media-like (dashes) and fat-like (line) adventitial conductivity outside the EEL. (D) Temperature profiles extending from the electrode toward the location of maximal power 10, 20 and 30 sec after the onset of RF delivery, with (lines) or without (dashes)

blood flow added to the model. In (C)–(D), the EEL is located at the interface of the pink (media) and the white (periadventitia) areas. (E, F) Plots of time averaged temperatures above 43.5°C at the end of 30 sec with (E) or without (F) modeling of blood flow define connected zones of injury. Gray circles in panels A–B, E–F depict electrode locations.

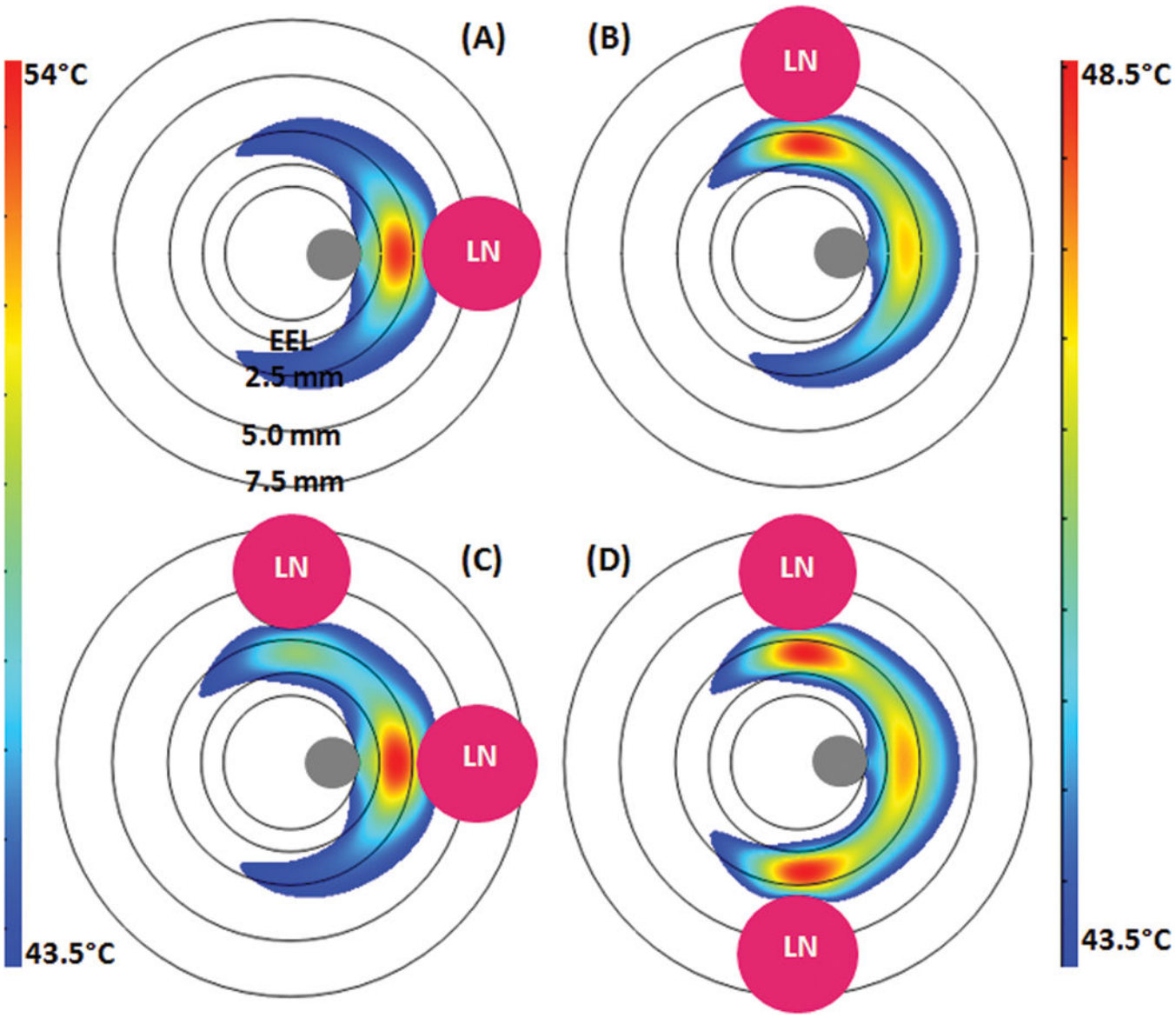

Figure 3. Model-predicted ablation geometries are influenced by the presence of peri-arterial lymph nodes

Simulated ablation geometries for conventional single electrode treatments with one (A,B) or two (C, D) lymph nodes (LN, pink). Lymph nodes were idealized as circles of uniform radius (2.5 mm), placed 3 mm from the lumen. The left scale bar pertains to panels (A, B), the right to panels (C, D).

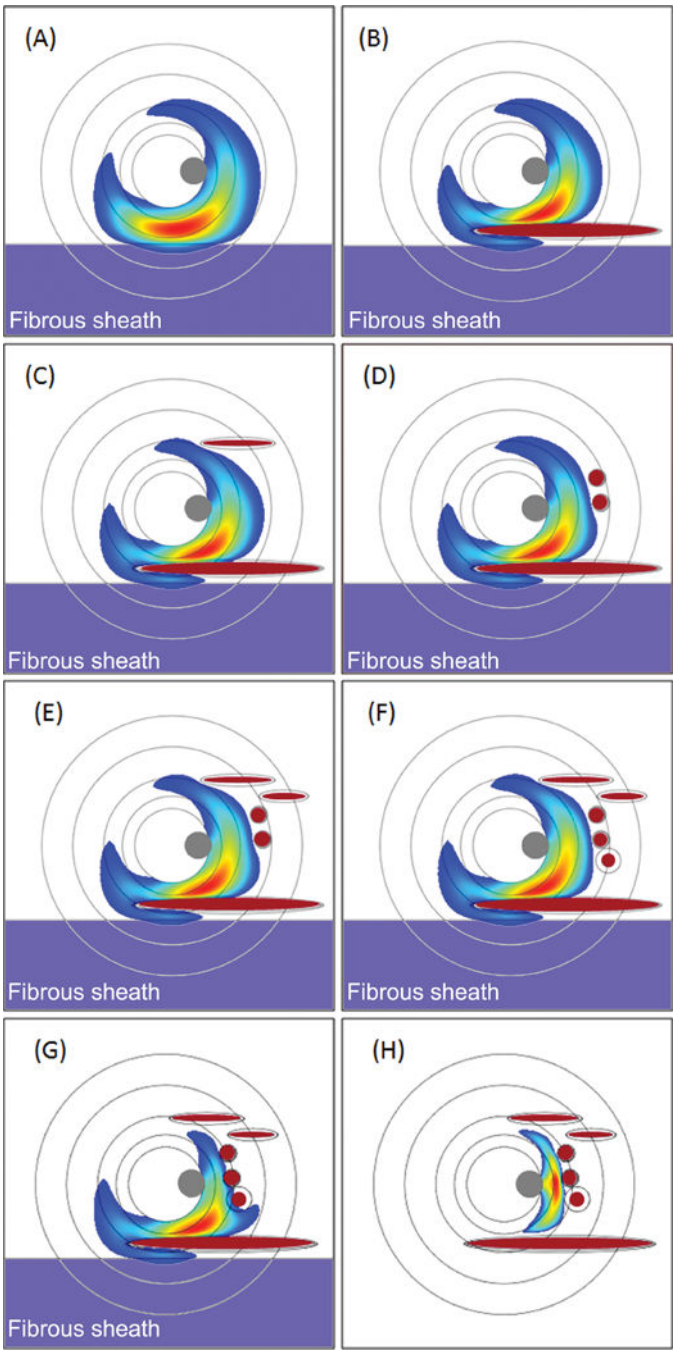

Figure 4. Predicted influence of peri-arterial anatomy on ablation geometry

Simulated ablation geometries for non-irrigatd single-electrode treatments of a range of model tissue anatomies. (A) The baseline computational geometry included a fibrous sheath (purple) in a lateral position relative to the electrode (gray). (B–F) The predicted influence of adding combinations of 1–5 lateral and distal blood vessels (red lumens). (G, H) The influence of shifting the blood vessels closer to the treating electrode in the presence (G) or absence (H) of a lateral fibrous sheath.

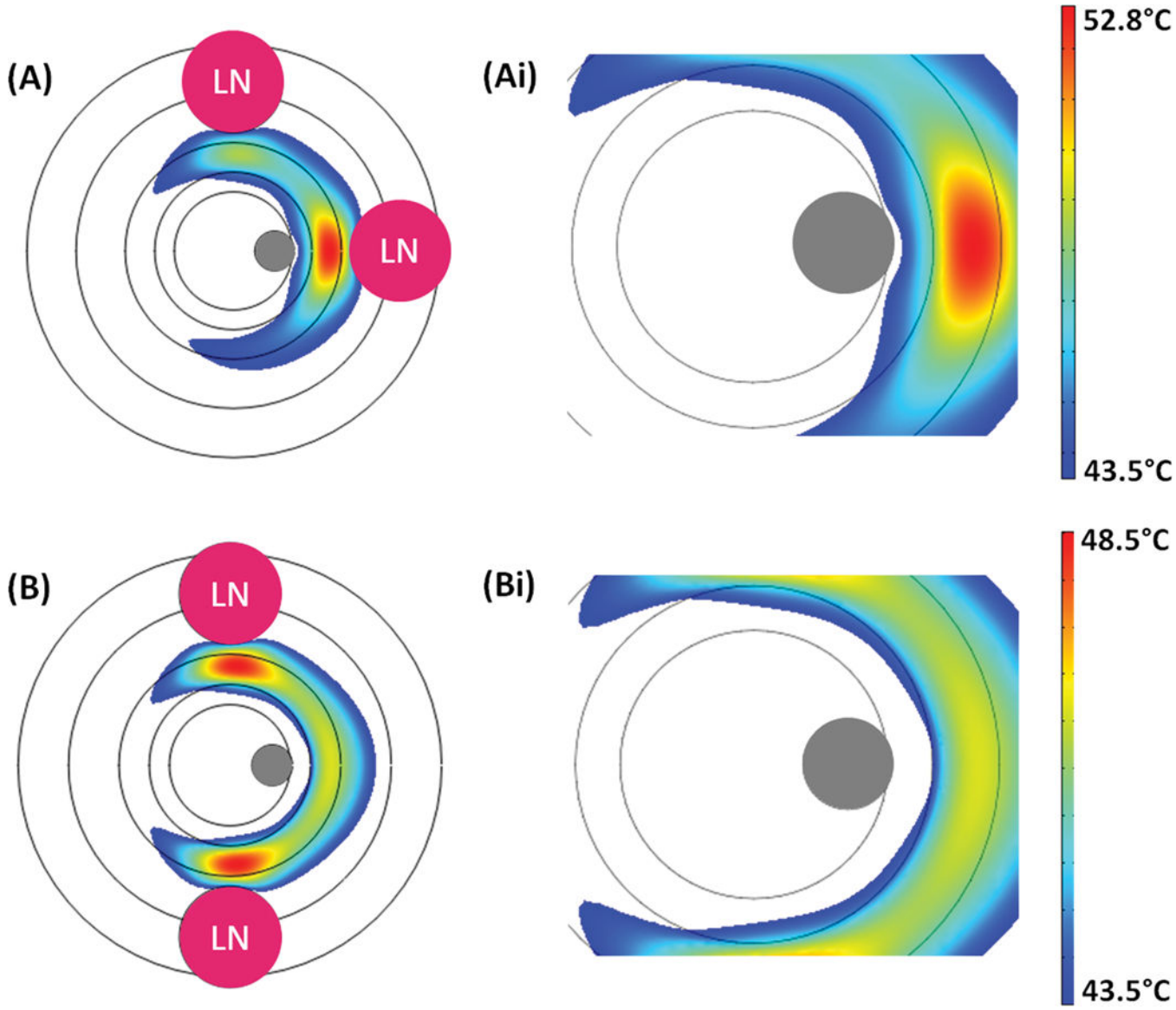

Figure 5. Model-predicted influence of local saline irrigation on ablation geometries

Ablation geometries depend on the context, in this case the position of adjacent lymph nodes (LN, pink). Simulated ablation geometries for irrigated single electrode (gray) treatments of a model tissue with one lateral and one distal lymph node (A) or two lateral lymph nodes (B). (Ai) and (Bi) depict higher magnification views of (A) and (B), respectively.

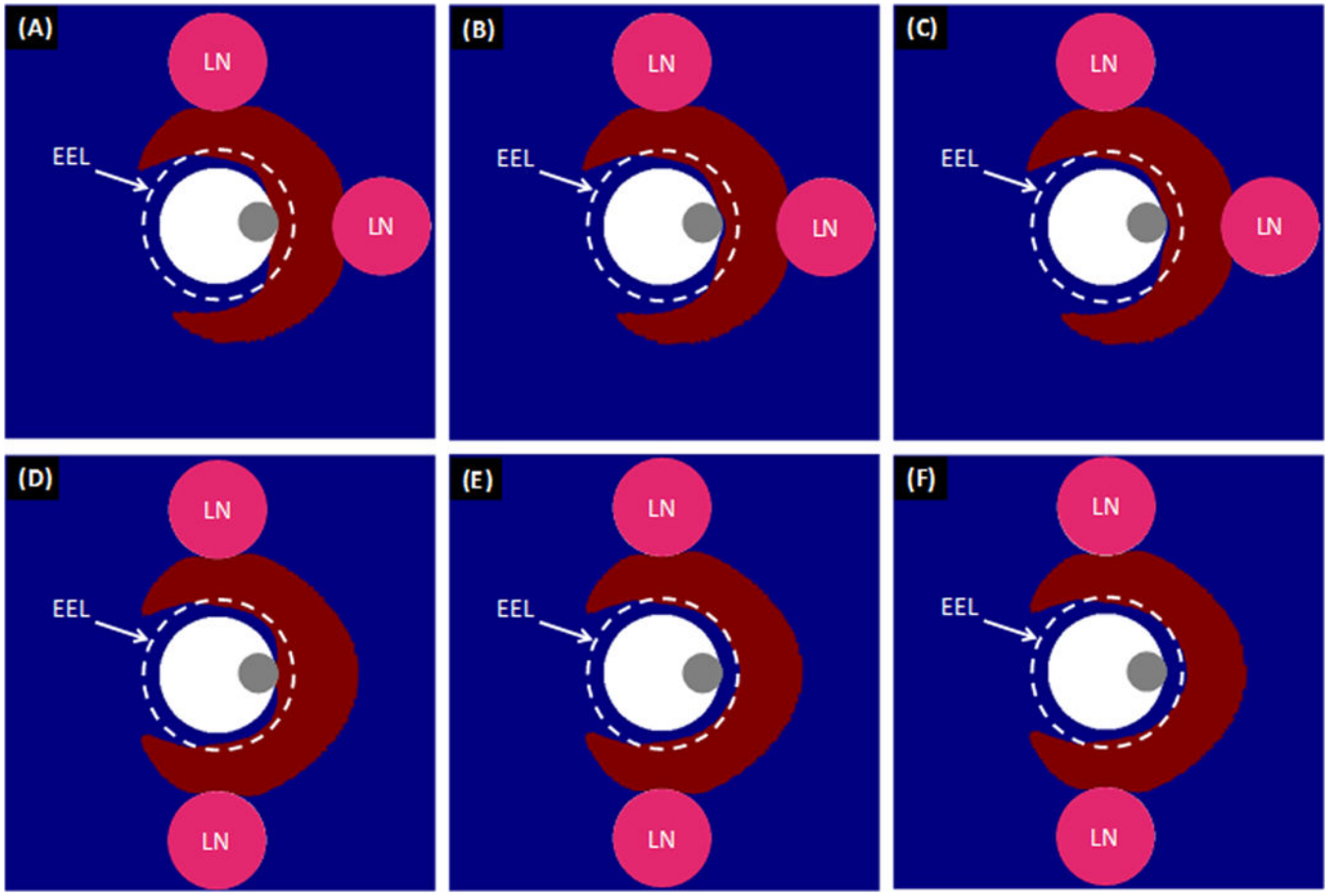

Figure 6. Sensitivity of model-predicted, artery wall protection to the rate of saline irrigation

Viable tissue (blue) and injured tissue (red) are shown for two lymph nodes (LN, pink), one lateral and one distal (top) or both lateral (bottom) after 30-sec single-electrode (gray) ablations (A, D) without saline irrigation, (B, E) with saline irrigation at the mural convection rate of blood or (C, F) with saline irrigation at double the mural convection rate of blood.

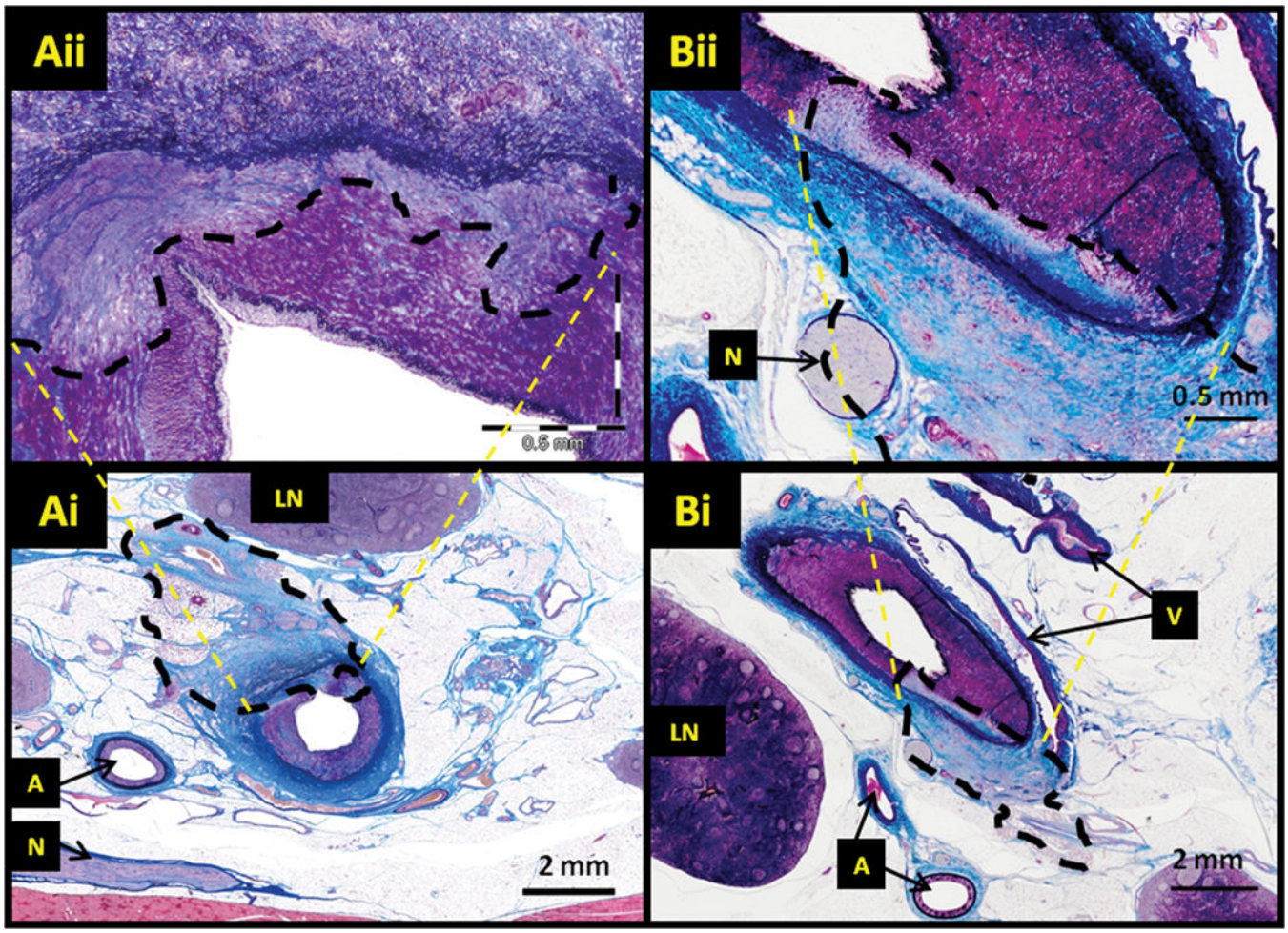

Figure 7.

Irrigation protects the arterial wall treatment site. Three Yorkshire swine arteries underwent discrete electrode irrigated treatments. (Ai, Bi) Traced maximal ablation zones (black dashes) overlaid on micrographs (Masson's trichrome stain) sections of two discrete electrode irrigated treatments sites along the same renal artery. (Aii, Bii) The corresponding high magnification images demonstrating preservation of inner tunica media and necrosis restricted to the outer media. Note how the ablation zones in Ai and Bi end abruptly at the periphery of neighboring lymphatic and vein, respectively.

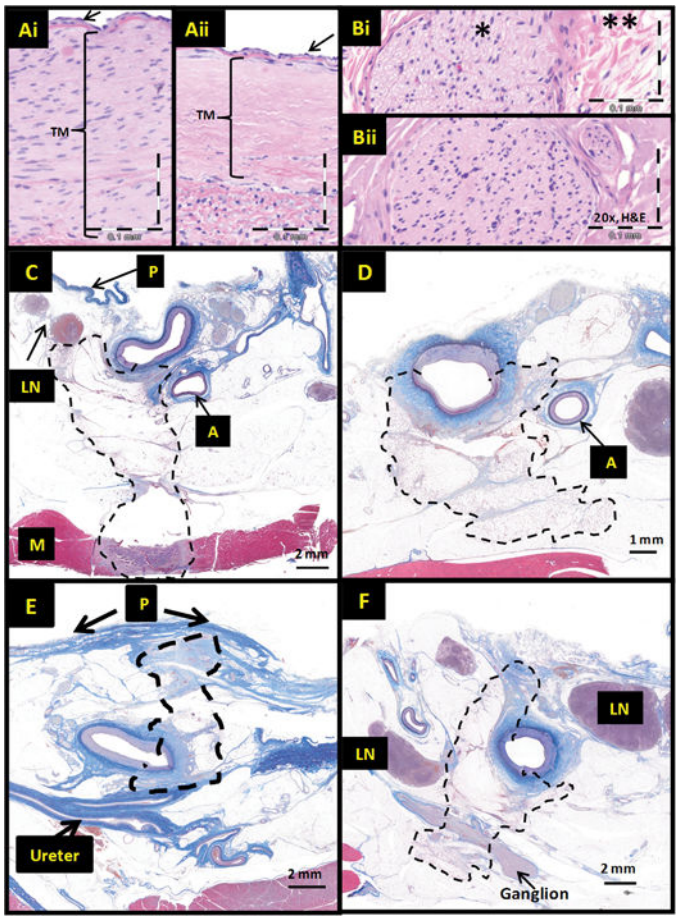

Figure 8. Maximal ablation zones of 5-electrode irrigated treatments in Yorkshire swine arteries

Overall, 8 Yorkshire swine arteries and 8 Yucatan swine arteries underwent irrigated 5-electrode treatments. (Ai) Untreated arterial segment demonstrating intact endothelium (arrow) and diffusely viable tunica media (thickness indicated by bracket). (Aii) Treated arterial segment exhibited diffusely necrotic (bracket), thinned tunica media (TM), with complete re-endothelialization (arrow) and no evidence of neointima. (Bi) Untreated nerve (asterisk) and surrounding adventitial collagen (double asterisk). (Bii) Treated, diffusely necrotic nerve with surrounding denatured collagen. (C–F) Four examples of traced maximal ablation zones illustrateing the approximate extent of treatment (dashed lines) and relationship to muscle (M), lymph nodes (LN), peritoneum (P) and arterial branch (A). Note how ablation zones seem to be drawn by neighboring HCAS such as lymph nodes and skeletal muscles (C–E) and excluded by neighboring blood vessels (in C–E).

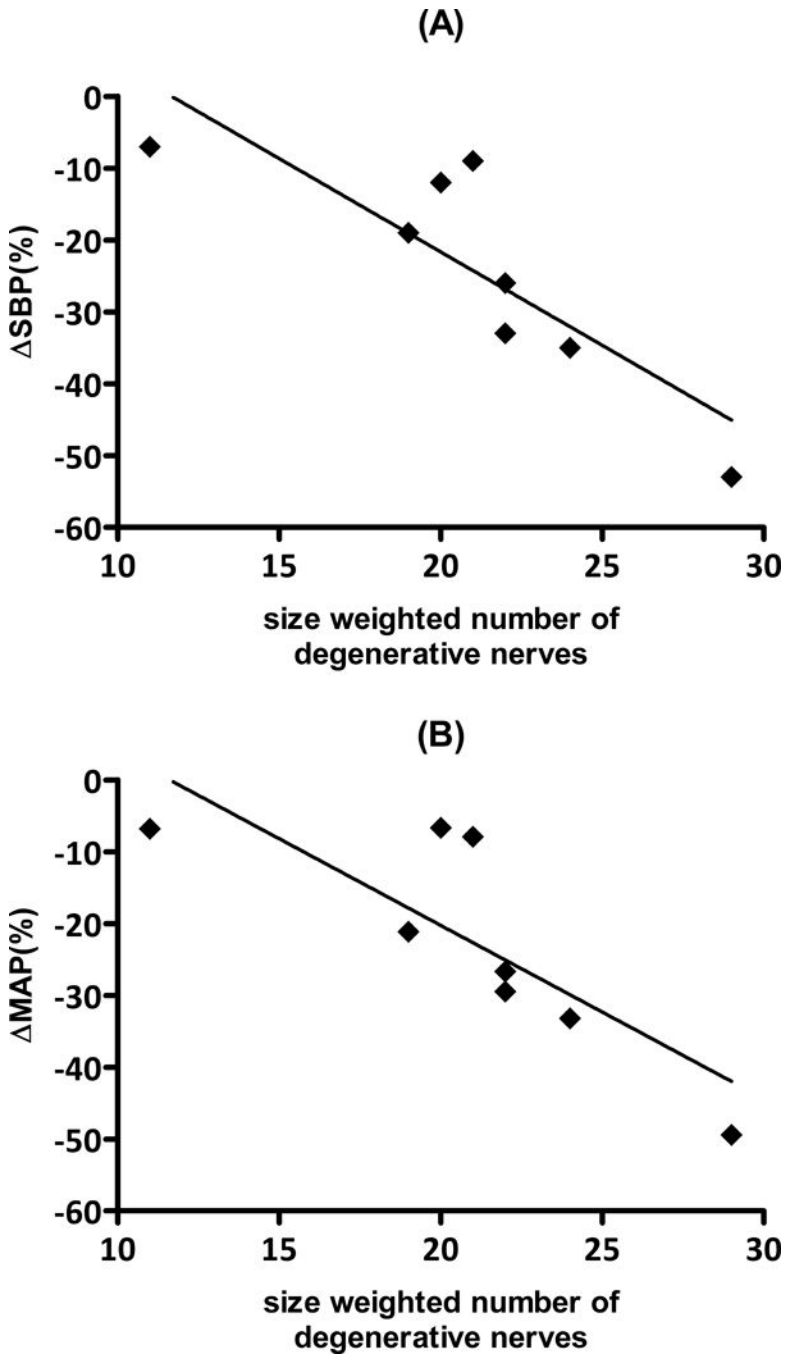

Figure 9.

Effect of unilateral, 5-electrode irrigated treatments on BP. After 7 days, 8 out of 10 Yucatan swine exhibited a reduction (**Full data set provided in** Table S2). Normalized reductions in SBP (A) and MAP (B) linearly track with the size weighted number of injured nerves per artery (Eq. 4). Experimental values (diamonds) are well approximated by linear regression (lines) in (A, R^2=0.70) and (B, R^2=0.65).

Table 1

Characterization of lesion geometry and affected nerves in sections with maximal ablation zones 7 days after discrete electrode treatments of Yorkshire swine. Values are mean (standard deviation).

	Irrigated[a]	Non-irrigated[b]
Ablation zone		
Area (mm^2)	11.3 (6.5)	22.5 (10.8)
Width (mm)	3.8 (2.4)	6.1 (2.3)
Depth (mm)	4.4 (1.3)	4.3 (1.1)
Nerves		
Total number	86.0 (79.6)	135.0 (64.2)
% Inside ablation zone	31.6 (16.3)	33.9 (9.5)
% Affected inside ablation zone	100 (0)	100 (0)
% Affected outside ablation zone	15.0 (15.9)	14.5 (7.6)
% Affected Total	40.2 (24.8)	43.0 (13.0)

[a] Based on 5 out of 6 irrigated single electrode treatments due to a tissue processing articfact at one of the treatment sites.

[b] Based on 6 of 7 non-irrigated single electrode treatments, discarding a treatment that was near a bifurcation and affected both branches.